Rock Mechanics and Rock Engineering (2024) 57:5783–5800
https://doi.org/10.1007/s00603-024-03840-7

ORIGINAL PAPER

Determination of the Rock Mass Bearing Mechanism Following Excavation of Circular Tunnels

Kaimeng Ma[1,2] · **Jichun Zhang**[1] · **Junru Zhang**[1] · **Jimeng Feng**[1] · **Ping Zhou**[3] · **Chao Kong**[4]

Received: 12 July 2023 / Accepted: 27 February 2024 / Published online: 3 April 2024

Abstract

The self-supporting capacity of the surrounding rock mass is a critical factor in maintaining tunnel stability after excavation and is a key determinant of tunnel support structures safety. Despite being widely applied, the mechanism behind the self-supporting effect remains a challenging issue to clarify. In this paper, we have used the finite difference method (FDM) to investigate the formation mechanism and characteristics of the surrounding rock mass's self-supporting zones. By analyzing the redistribution of a stress and an energy using stress concentration factor, energy concentration factor, we propose a self-supporting mechanism of the surrounding rock mass under different horizontal to vertical stress ratios. The further analysis results were subsequently validated through non-contact strain acquisition experiments. Our findings suggest that in cases of unequal horizontal and vertical stress, a “primary load-bearing zone” is formed in the direction of the vertical maximum principal stress within the rock mass. The rock mass areas aligned parallel to the direction of the maximum principal stress transfer the maximum principal stress to the primary load-bearing zone, causing compression towards the “primary load-bearing zone” and resulting in the formation of a “passive load-bearing zone”. The primary load-bearing zone resembles the footings of an arch, while the passive load-bearing zone resembles the arch's intrados. When the horizontal and vertical stresses are equal, the formation of the self-supporting zone is caused by the radial deformation of the surrounding rock into the tunnel cavity, followed by the mutual compression of the surrounding rock in the circumferential direction. The surrounding rock mass quality and depth of burial influence the size of the self-supporting zone, with the surrounding rock mass quality having a greater impact than the depth of burial.

Highlights

- An analysis has been conducted to examine the differences between stress and energy redistribution after a tunnel excavation.
- An investigation has revealed the mechanism behind the formation of two types of load-bearing arches, namely the "arch base supporting wedge-shaped arch" and the "compression around to the middle", under different conditions after tunnel excavation.
- The influence of horizontal to vertical stress ratio, overburden depth and rock mass level on the extent and bearing capacity of the self-supporting zone is analyzed.

Keywords Tunnel engineering · Load-bearing zone · Load-bearing mechanism · Redistribution

---

✉ Jichun Zhang
jczhang2004@126.com

✉ Junru Zhang
jrzh@swjtu.edu.cn

[1] School of Civil Engineering, Southwest Jiaotong University, Chengdu 610031, China

[2] School of Civil Engineering, Shijiazhuang Tiedao University, Shijiazhuang 050043, China

[3] Faculty of Geosciences and Environmental Engineering, Southwest Jiaotong University, Chengdu 611756, China

[4] School of Civil Engineering and Architecture, Southwest University of Science and Technology, Mianyang 621000, China

1 Introduction

The arch is designed to transfer the weight from the top to the ground to withstand greater pressure when the upper part is also under pressure. This characteristic has made arch structures popular in a wide range of projects, including domes, arch bridges, and tunnels. In the field of tunnelling, Ritter (1879) first proposed a model for a naturally balanced arch under self-weight loading. Later, Janssen (1895) explained the grain bin effect and developed an analytical formula, which formed the basis for the tunnel arch effect. Terzaghi (1946) completed the Trapdoor test and proposed a model for the settlement caused by tunnel construction. Since then, numerous researchers in underground engineering have studied the bearing capacity of the surrounding rock mass (Handy 1985; Tien 1996; Chen et al. 2011). It is now well-established that the surrounding rock mass acts as both the load for the tunnel structure and the support for the tunnel. The shape of the pressure arch after tunnel excavation has a significant impact on the stability of the tunnel structure (Zhou et al. 2022a; Li et al. 2014).

Although the self-supporting capacity of the surrounding rock mass in a tunnel is real, it is elusive and cannot be observed directly in a construction project. Researchers have employed various methods to investigate this phenomenon, including the finite element method (Huang et al. 2002; Keawsawasvong and Ukritchon 2020), the discrete element method (Chen et al. 2020; Wang et al. 2021), theoretical analysis (Lin et al. 2022a; Dancygier et al. 2016), and model testing (Wang 2007; Iglesia et al. 2014). Chevalier et al. (2012) discovered that the shearing strength of the material was the key factor in load transfer by conducting Trapdoor tests with different materials under varying stress conditions. Lin et al. (2022b) used theoretical, experimental, and numerical methods to compare stress transfer mechanisms in circular and rectangular tunnels, correcting pressure arch distribution by accounting for differences in overburden depth and internal friction angles. Huang et al. (2002) was the first to propose a method for determining the pressure arch boundary following tunnel excavation, which Liang (2006) used to identify the range of pressure arches as the portion with tangential stress greater than the original stress, forming the basis for current research on pressure arch ranges. Kong et al. (2018) analyzed the effects of varying overburden depth, surrounding rock mass conditions, and stress ratios on the bearing arch at the top of the tunnel. Ma et al. (2022a) employed complex variable functions and slip line theory to estimate the elastic and plastic stress fields and determine the range of the bearing arch after tunnel excavation. Li (2016) proposed a method for predicting the arch effect during tunnel construction by comparing the height of pressure arches. Moreover, pressure arches have been observed in special strata (Zhou et al. 2022b), such as aeolian (Ma et al. 2022b) sand and loess (Xu et al. 2021), using reinforcement techniques.

Extensive research has been conducted on pressure arches in tunnels, including the formation conditions (Yang et al. 2015), extent, dynamic adjustment (Ye et al. 2019), and boundary conditions affecting pressure arches. These findings have guided tunnel design concepts and provided theoretical support for construction methods. However, despite these achievements, the theoretical research of self-supporting surrounding rock system has lagged behind the practical application, leaving no clear conclusion on the mechanism of self-supporting arch after excavation. In the soils, the bearing arch was mainly formed by gravity and friction of soils. In the rock mass, the bearing arch is formed by the wedge tightening of the rock mass moving towards the cavity. However, how they were wedged was unknown, and whether the wedge tightening of the bearing arch was the same under different boundary conditions was also uncertain. Additionally, previous studies on the bearing arch primarily focused on the redistribution of tangential stress, neglecting changes in the elastic strain energy of the surrounding rock mass. To address this gap, finite difference numerical calculations were employed, and stress-energy criteria were considered to analyze the load-bearing arch formation mechanism of a deeply buried circular tunnel after excavation and to examine the effect of boundary conditions on the self-supporting zone. Finally, experimental tests were conducted to analyze the stress concentration around tunnels under different horizontal to vertical stress ratios, to validate the surrounding rock mass's load-bearing mechanism.

2 Problem Description

The surrounding rock mass serves both as a source of load and as a load-bearing structure for tunnels. The load originates from the extrusion of the surrounding rock mass into the cavity due to tunnel excavation and unloading. The self-supporting zone, which forms after tunnel excavation, is created by the autonomous adjustment of the surrounding rock mass as it resists deformation. The self-supporting mechanism of the surrounding rock mass plays a critical role in the tunnel's stability, while support structures are primarily used to quickly regulate the balance of stresses in the surrounding rock mass. The self-supporting zone in tunnels is the stress concentration zone formed by the deflection of stresses in the surrounding rock mass due to the unloading effect. This zone is characterized by an increase in tangential stresses to carry radial loads, which is similar to the form of forces in an arch bridge. Therefore, it is referred to as the bearing arch or pressure arch. The widely accepted definition for the self-supporting zone is the area where the tangential stress

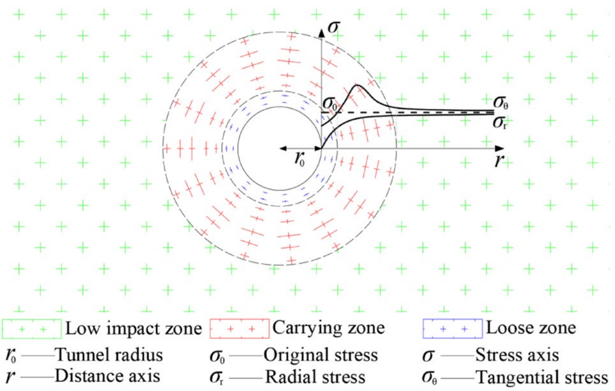

Fig. 1 Stress state distribution around the tunnel

exceeds the original rock stress. After tunnel excavation, the surrounding rock mass can be divided into three zones: the relaxed zones, the self-supporting zones, and the low-impact zones, as shown in Fig. 1. If the surrounding rock mass conditions are good or the ground stress magnitude is low, the loose zone disappears, and the self-supporting zone is located at the tunnel boundary. As the depth of burial is further reduced, the top of the tunnel is unable to form a self-supporting zone, leading to a collapse.

To facilitate analysis, the stress concentration factor is defined by Eq. (1). If the D_σ is greater than 0, the surrounding rock mass has a self-supporting zone. When it is less than 0, the surrounding rock mass does not have a self-supporting zone. Using Kong's stress criterion (Kong et al. 2018), $D_\sigma = 0$ is regarded as the inner boundary of the load-bearing zone, while $D_\sigma = 0.1$ is taken as the outer boundary.

$$D_\sigma = \frac{\sigma_\theta - \sigma_\theta^0}{\sigma_\theta^0}, \tag{1}$$

where D_σ is the stress concentration factor, σ_θ is the tangential stress, σ_θ^0 is the initial tangential stress.

At a certain depth of burial, the rock can be considered an elastic medium in a compacted state, which accumulates a certain elastic strain energy under long-term loading. After tunnel excavation, this stored elastic strain energy is released, and work is done. Thus, in addition to the redistribution of stresses, the energy around the tunnel is also redistributed. It has been demonstrated that the redistribution of energy after tunnel excavation is related to the direction of the principal stresses (Zhu et al. 2003). Furthermore, the two quadrants parallel to the main stress field are energy release zones, while the two quadrants perpendicular to the main stress field are energy gathering zones (Zhu et al. 2003), as shown in Fig. 2. However, there have been limited investigations on the relationship between energy and the load-bearing zone. Li (2010) and Zhu et al. (2003) have mentioned relevant studies, but no in-depth analysis has been conducted. The formation mechanism of bearing zone and the influencing factors of spatial shape were investigated. At present, the academic community mainly defined the bearing zone from the perspective of stress deflection, and this paper also continued this criterion. In the process of stress redistribution, the stress in the rock would deflect in different directions in some parts, and the deflection angle would change with different positions. If it was only reflected from the stress state, it was necessary to consider the three elements of the force (a vector), which was very complex. At the same time, the stress of rock mass was three-dimensional (except for the tunnel boundary). The elastic strain energy of rock mass could consider the principal stresses in three directions, and it was a scalar. Its increase or decrease could reflect the different properties of rock mass. The bearing area was the area where the rock mass outside the tunnel bears in-situ stress, and the state of this part of rock mass was different from the original state. Therefore, by means of elastic strain energy, the formation mechanism of bearing area after tunnel excavation was studied.

The elastic strain energy that can be accumulated by the surrounding rock mass is shown in Eq. (2). The long tunnel can be considered as a plane strain problem with ε_2=0. However, intermediate principal stresses have a non-negligible influence in tunnels. Substituting Hooke's law Eq. (3) into (2) and simplifying the principal stresses gives the elastic strain energy equation after tunnel excavation as Eq. (4).

$$U^e = \frac{1}{2}\sigma_{ij}\varepsilon_{ij} = \frac{1}{2}\begin{pmatrix} \sigma_{xx} & \sigma_{xy} & \sigma_{xz} \\ \sigma_{yx} & \sigma_{yy} & \sigma_{yz} \\ \sigma_{zx} & \sigma_{zy} & \sigma_{zz} \end{pmatrix}\begin{pmatrix} \varepsilon_{xx} & \varepsilon_{xy} & \varepsilon_{xz} \\ \varepsilon_{yx} & \varepsilon_{yy} & \varepsilon_{yz} \\ \varepsilon_{zx} & \varepsilon_{zy} & \varepsilon_{zz} \end{pmatrix}, \tag{2}$$

$$\begin{cases} \varepsilon_{xx} = \frac{1}{E}\left[\sigma_{xx} - \nu\left(\sigma_{yy} + \sigma_{zz}\right)\right] \\ \varepsilon_{yy} = \frac{1}{E}\left[\sigma_{yy} - \nu\left(\sigma_{xx} + \sigma_{zz}\right)\right] \\ \varepsilon_{zz} = \frac{1}{E}\left[\sigma_{zz} - \nu\left(\sigma_{yy} + \sigma_{xx}\right)\right] \end{cases}, \tag{3}$$

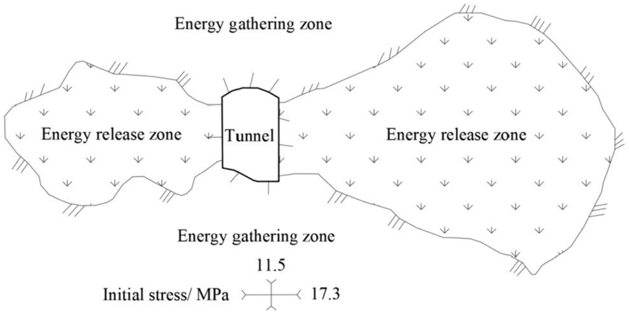

Fig. 2 Loading and unloading areas around the cavern (Zhu et al. 2003)

$$U^{\mathrm{e}} = \frac{1}{2E}\left[(\sigma_1^2 + \sigma_3^2 - \nu(2\sigma_1\sigma_3 + \sigma_2\sigma_3 + \sigma_1\sigma_2)\right], \tag{4}$$

where U^{e} is the elastic strain energy, σ_{ij} is the Cauchy stress, ε_{ij} is the strain, σ_1 is the major principal stress, σ_2 is the intermediate principal stress, σ_3 is the minor principal stress, E is the elastic modulus, ν is the Poisson's ratio.

Similarly, the energy concentration factor is defined as in Eq. (5). Energy gathers when the D_{u} is greater than 0. And it decreases when the energy carrying capacity is less than 0. $-0.1 < D_{\mathrm{u}} < 0.1$ is defined as a small impact area, which can be considered as no impact area.

$$D_u = \frac{U^{\mathrm{e}} - U_0^{\mathrm{e}}}{U_0^{\mathrm{e}}}, \tag{5}$$

where D_{u} is the energy concentration factor, U_0^{e} is the initial elastic strain energy.

3 Research Methods

3.1 Numerical Model

3.1.1 Description of Calculation Model

To investigate the mechanism of load-bearing zone formation and its influencing factors, a numerical study was conducted by considering various parameters. The finite difference calculation software (FLAC 3D) was used, and the following assumptions were made: (1) the surrounding rock mass was considered as an ideal elasto-plastic continuum, and the Mohr–Coulomb strength criterion was applied, and (2) three directions of principal stresses (vertical, horizontal, and longitudinal) were considered as boundary conditions for the model. When strain softening model were used, the plastic state was shortened. Under the same conditions, both the inner and outer boundaries of the bearing zone would move towards the interior of the surrounding rock mass (Cui et al. 2023; Yi et al. 2020, 2021). However, it did not affect the mechanism of determining the formation of the bearing zone. Therefore, the Mohr–Coulomb strength criterion was adopted. The model dimensions were 200 m (horizontal) × 200 m (vertical) × 1 m (longitudinal), with displacement fixed boundaries and stress boundaries. The displacement fixed boundaries were set at the front, back, left, right, and bottom of the model. The gravity of the surrounding rock mass was considered, and the tunnel was assumed to be circular with a radius of 5 m.

In all analyses, full-section excavation was assumed, and the effects of the excavation process were disregarded. The excavation method was found to have little impact on the extent of the pressure arch (An et al. 2022; Zhang et al. 2014). Additionally, the influence of the support structure was not considered, and only the self-supporting behavior of the surrounding rock mass was analyzed. The calculation involved a two-step process. First, the initial equilibrium was performed, where all elements and boundary conditions were activated, and grid displacements and accelerations were cleared once the calculation had converged. Second, the elements within the tunnel were removed, and the equilibrium was calculated without changing the boundary conditions. A maximum unbalanced force of less than 10^{-5} was used as a convergence criterion. To measure the stress distribution after excavation, 13 measuring lines, each 60 m long and 15° apart, were located perpendicular to the tunnel perimeter. The grid was set in a 60 m circle around the tunnel, with a 1 m radial direction, and the external grid dimensions were mapped to the model boundary. Only one layer of mesh was set in the longitudinal direction, and the model is presented in Fig. 3. Due to the influence of gravity, the model exhibited different vertical stresses at different heights. After calculating with the k value, the horizontal stress on the model boundary gradually increased with burial depth. Displacement boundaries and stress boundaries were set in the longitudinal direction to ensure stress and no strain.

3.1.2 Working Conditions and Parameter Selection

The mechanism and variation of the load-bearing zone in the tunnel's surrounding rock mass were obtained by adjusting the surrounding rock mass parameters and ground stress levels. The parameters for the rock mass were taken from the "Chinese Railway Tunnel Design Code" for Grade IV and V surrounding rock mass (National Railway Administration of the People's Republic of China 2016), which covers most of the strata susceptible to deformation. The Code categorizes the surrounding rock mass through a combination of qualitative descriptions and BQ values, with six grades ranging from Grade I (best) to Grade VI (worst). The BQ values took into account the uniaxial saturated compressive strength of the rock and the integrity of the rock mass, and the calculation formula was shown in Eq. (6). Grade IV includes fractured hard rock mass or relatively intact soft rock mass with a BQ of 251 to 350, while Grade V includes fractured soft rock mass, among others, with a BQ of less than 250. The IV grade surrounding rock mass corresponds to Q values of 0.4–4, while the V grade surrounding rock mass corresponds to Q values of 0.1–0.4 (Wu et al. 2023). Combining the size of the model with the adaptability of the range of the bearing area, suitable elastic moduli were determined to study the variation pattern of the bearing area. The surrounding rock mass parameters are listed in Table 1. Overburden depths of 100 m, 300 m, and 500 m were selected, with vertical stresses applied to the top of the model where they exceeded the model dimensions. This range of overburden depths was relatively common and concentrated some large deformations in the tunnel. The vertical ground stress scale ranges from 2 to 10 MPa, and the horizontal stresses include Poisson effects and tectonic stresses, with horizontal to vertical stress ratios of 0.5, 1.0, and 1.5. There are three relationships between vertical stress and horizontal stress: horizontal stress is less than vertical stress, horizontal stress is equal to vertical stress, and horizontal stress is greater than vertical stress. The ratio of horizontal to vertical stress is 0.5, 1.0, 1.5 to represent the three relationships between horizontal and vertical stress. The horizontal to vertical stress ratio k is defined in Eq. (7), and the 18 working conditions are presented in Table 2.

$$BQ = 100 + 3R_c + 250K_v, \tag{6}$$

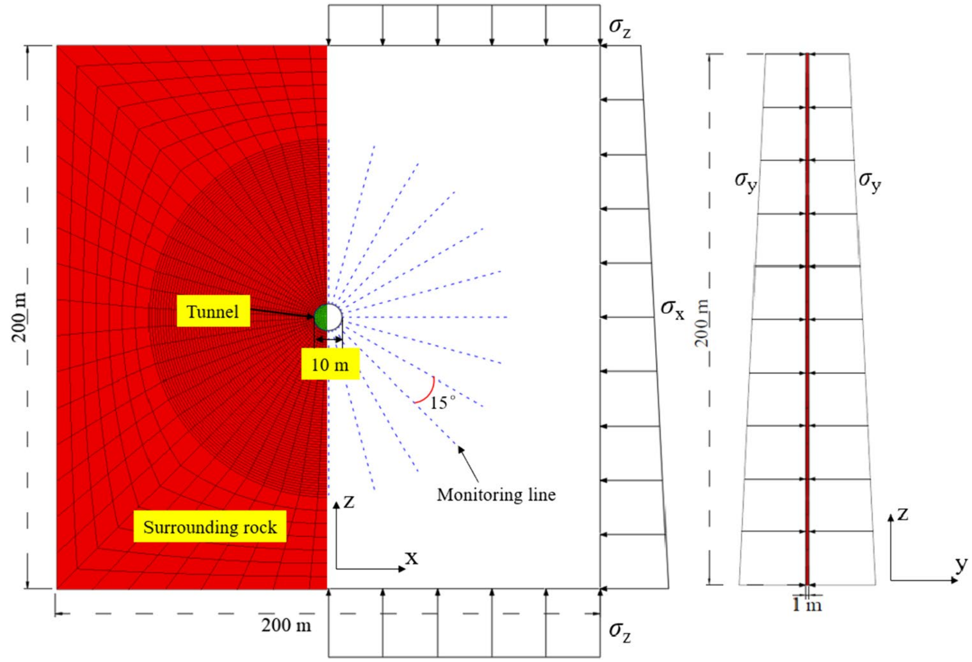

Fig. 3 Numerical model

Table 1 Calculation parameters

Surrounding rock mass grade	Q value	Density (kN/m^3)	Elastic modulus (GPa)	Poisson	Cohesion (kPa)	Friction (°)
IV	0.4–4	21.50	36.5	0.3	450	33
V	0.1–0.4	18.50	15	0.35	200	27

Table 2 Working condition

Condition number	Rock cover (m)	Grade	k	Condition number	Rock cover (m)	Grade	k	Condition number	Rock cover (m)	Grade	k
IV1a	100	IV	0.50	IV1b	100	IV	1.00	IV1c	100	IV	1.50
IV3a	300	IV	0.50	IV3b	300	IV	1.00	IV3c	300	IV	1.50
IV5a	500	IV	0.50	IV5b	500	IV	1.00	IV5c	500	IV	1.50
V1a	100	V	0.50	V1b	100	V	1.00	V1c	100	V	1.50
V3a	300	V	0.50	V3b	300	V	1.00	V3c	300	V	1.50
V5a	500	V	0.50	V5b	500	V	1.00	V5c	500	V	1.50

where BQ is the basic quality index value of surrounding rock mass, R_c is the uniaxial saturated compressive strength of the rock, K_v is the integrity of the rock mass.

$$\sigma_{\mathrm{z}} = \sigma_{\mathrm{y}} = \frac{1}{k}\sigma_{\mathrm{x}} \tag{7}$$

3.2 Test Design

3.2.1 Test Overview

The experiment employed the XTDIC (eXtended Three-Dimensional Digital Image Correlation) system for full-field deformation measurement and analysis. This system captures speckle patterns on the surface of the observed object throughout the entire process using high-precision cameras. The DIC algorithm is utilized to obtain the disparity data of each point on the surface of the observed object, reconstructing the coordinates of the speckle pattern. By comparing the differences in speckle pattern coordinates within the measurement area, the strain field is obtained, enabling the analysis of the corresponding stress field. Just as formula 1 and formula 5, the main analysis of elastic strain energy and stress in this paper is the rate of change. Although the initial energy and stress are affected by gravity differently, when using formula 1 and formula 5 for calculation, D_σ and D_u are 0. D_σ and D_u observed after tunnel excavation are an effect of redistribution. Although the influence of gravity is not considered in the test, the initial D_σ and D_u is also 0. The change process recorded by the camera through the scatter plate is in line with this rate of change. This process is difficult to be recorded in the numerical simulation and the actual situation, so the quantitative model test is not selected in the test, but the qualitative verification test is selected. The horizontal loading form is determined (Zhou et al. 2019; Jeon et al. 2004).

The experiment aimed to obtain surface strain data of the specimen. A horizontal loading configuration was utilized, disregarding the influence of gravity. The specimen surface was secured using acrylic plates and steel bars to restrict vertical displacements, ensuring a planar strain pattern. Data acquisition was performed in a single-camera mode. The experimental hardware system was divided into a loading system and an image acquisition system. The schematic diagram of the setup is shown in Fig. 4a, while the on-site photograph is presented in Fig. 4b. The loading system comprised three jacks, three 1.5 cm-thick force-transmitting steel plates, and a reaction frame. The image acquisition system included a camera, a camera bracket, two light sources, and a monitor. A DeepVision Intelligent SH6-207-M-40 high-speed camera model was selected for the experiment, equipped with a Canon EF 16-35mm f/2.8L II USM full-frame wide-angle lens. The lens had a minimum focal length of 16 mm and a maximum aperture of 2.8. The camera bracket was positioned 1.3 m away from the specimen surface, ensuring complete capture of the specimen's surface in the images.

The physical size of the speckle is determined by the image scale and satisfies Eq. (8). In this experiment, the image resolution was 1440 × 1080 pixels, and the physical dimension of the component was 1 m. Therefore, the physical size of an 8-pixel speckle was 7.4 mm.

$$l_{\mathrm{d}} = \frac{p_{\mathrm{d}}}{\overline{D}}, \tag{8}$$

where l_{d} is the speckle size, p_{d} is the number of pixels, $\overline{D}$ is the image scale.

3.2.2 Working Conditions and Steps

Two test conditions were established, namely, four-way equal loading and loading mode with a principal stress direction. The test material chosen was M10 cement mortar. The design strength of M10 cement mortar is 10 MPa. The test conditions are presented in Table 3. The experiment adopted horizontal loading (without gravity influence), and the model was axisymmetric. The three types of geostress relationships could be simplified into two types, that was, the two directions of stress were equal and not equal. Therefore, there were two sets of horizontal to vertical stress ratio, where $k = 0.5$ represented the case of unequal stress in the two directions and $k = 1.0$ represented the case of equal stress in the two directions. Because this investigation is universal and there is no corresponding tunnel prototype, no model experiments were conducted. Furthermore, the proportion of experimental materials and tunnel dimensions was not taken into account. The main purpose of this experiment is to verify the stress changes around the tunnel, therefore, only a qualitative comparison was made between two significant principal stress directions in the working conditions.

The experimental procedure was conducted as follows: (1) Assembly of the specimens, (2) Mounting of the camera, (3) Connection of the equipment, (4) Adjustment of the image, (5) Gradual loading, (6) Image processing. During the pressurization process, it was observed that the ultimate strength between the reaction frame and the specimen was approximately 18 tons. When the loading exceeded 18t, the reaction frame underwent deformation, which could not guarantee the effective application of the load. Therefore, the graded loading levels adopted are shown in Table 4. The dimensions of the loaded specimen boundary were 1 m × 0.2 m, with an area of 0.2 m^2. The load quantities for the three graded levels were 5 tons, 10 tons, and 15 tons, corresponding to loading stresses of 250 kPa, 500 kPa, and 750 kPa, respectively.

Fig. 4 Test device

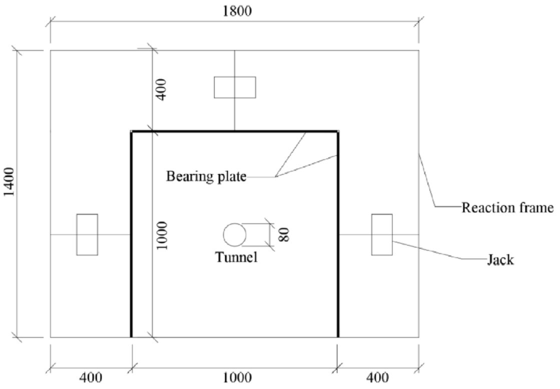

(a) Vertical diagram of experimental model (mm)

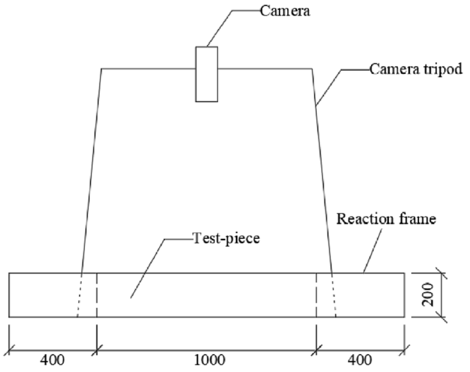

(b) Front view of experimental model (mm)

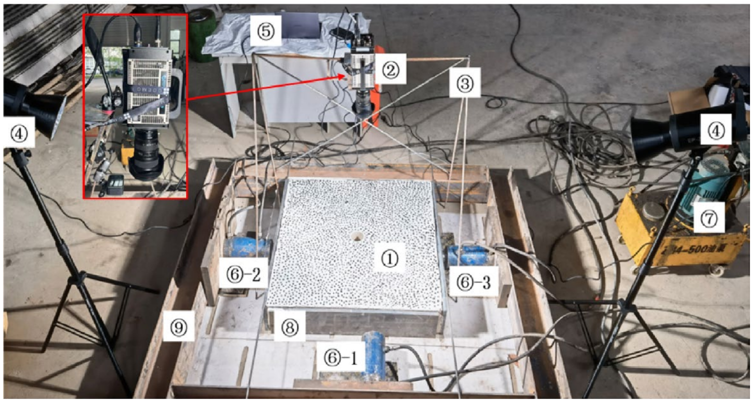

①—Test components, ②—High-speed camera, ③—Camera mount, ④—Lighting, ⑤—Monitor, ⑥-1、⑥-2、⑥-3—1#、2#、3# Jack, ⑦—Oil pump, ⑧—Bearing plate, ⑨—Reaction frame.

(c) Test photos

Table 3 Working condition

Number	Test materials	Horizontal to vertical stress ratio
A	M10 mortar	$k = 0.5$
B	M10 mortar	$k = 1$

4 Results and Discussion

4.1 Calculation Results

The stress concentration factor (D_σ) and energy concentration factor (D_u) were incorporated into the Fish language finite difference program to generate a partial cloud of stress carrying capacity as shown in Fig. 5, and a partial cloud of energy carrying capacity as shown in Fig. 6. A rock cover of 100 m for Grade V was chosen as an example to illustrate

Table 4 Hierarchical loading level

Number	Horizontal to vertical stress ratio	Loading level	1# Jack	2#, 3# Jack
A	$k=0.5$	First level loading	5 t	2.5 t
		Second level loading	10 t	5 t
		Third level loading	15 t	7.5 t
B	$k=1$	First level loading	5 t	5 t
		Second level loading	10 t	10 t
		Third level loading	15 t	15 t

the elevated lowering zone of stress and energy, which was found to be moderate in extent and easily identifiable. The stress redistribution was observed to be close in shape, with an approximately circular, symmetrical distribution for a horizontal to vertical stress ratio of 1. However, when the horizontal stress factor was not 1, the stress redistribution was found to be elliptical, with the long axis parallel to the direction of the major principal stress and stresses concentrated in the direction perpendicular to the major principal stress. The redistribution of energy showed considerable variation in shape. When the horizontal stress was equal to the vertical stress, the energy concentration was similar to the stress concentration, forming an approximately circular distribution. However, when the horizontal stresses were not equal to the vertical stresses, the area of elevated energy did not form a closed area, with a decrease in energy occurring in the area parallel to the large principal stresses and an increase in energy occurring in the direction perpendicular to the large principal stresses. Stress redistribution was the law of tangential stress redistribution after tunnel excavation. The change of energy was affected by the three principal stresses. The redistribution of energy of surrounding rock mass was a comprehensive analysis of the state of rock mass, so the redistribution of stress and energy was different.

To obtain the stress and energy carrying capacity at each point, the calculated stresses were input into Eqs. (1) to (5), and the representative results are shown in Fig. 7. The distribution pattern of the load carrying capacity with each angle had a strong correlation with the horizontal to vertical stress ratio. The depth of burial and the grade of the surrounding rock mass only affected the position of the boundaries and had little effect on the distribution pattern. The locations of

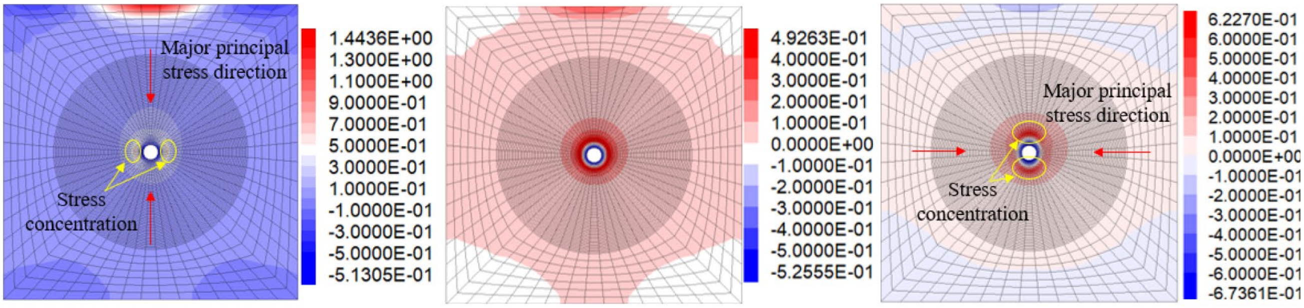

(a) Condition V1a (b) Condition V1b (c) Condition V1c

Fig. 5 Stress concentration factor cloud (D_σ)

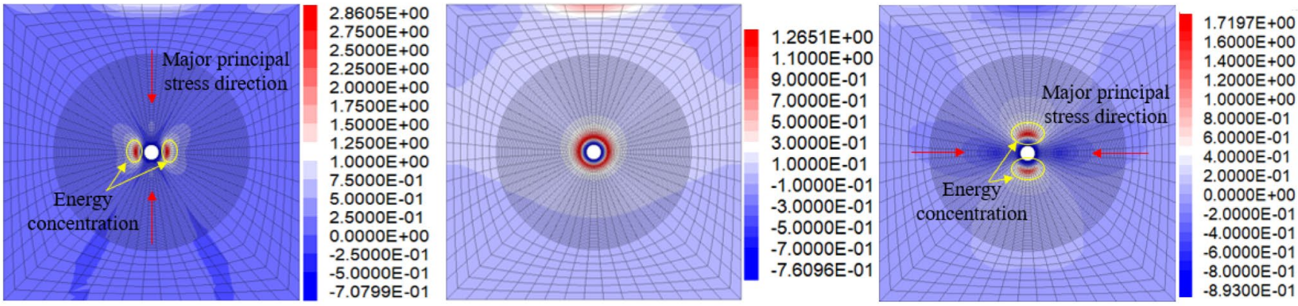

(a) Condition V1a (b) Condition V1b (c) Condition V1c

Fig. 6 Energy concentration factor cloud (D_u)

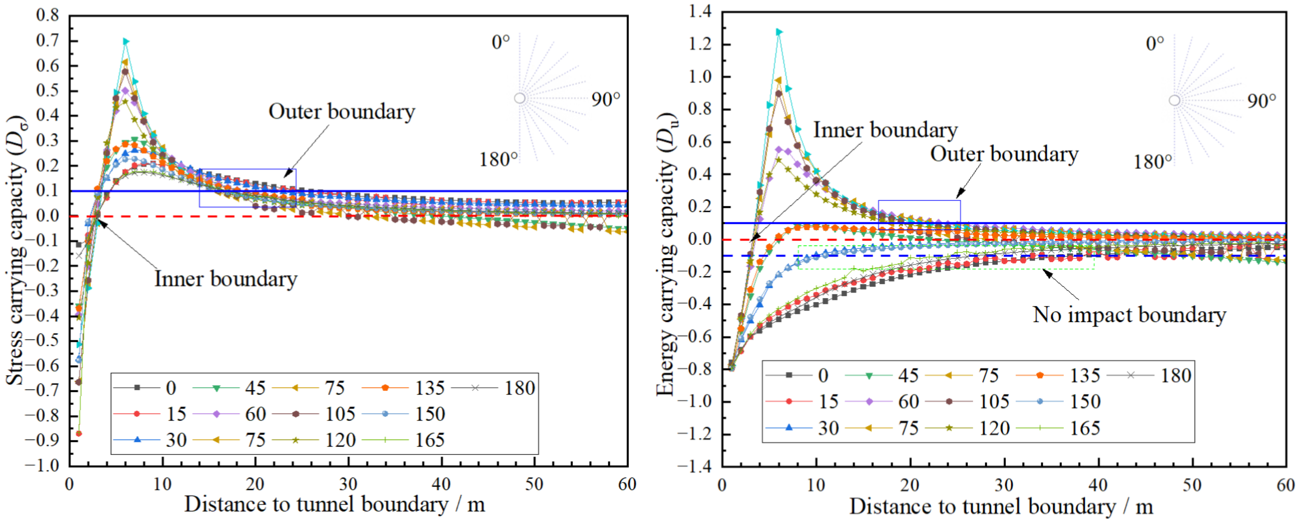

(a) Stress distribution (Condition V1a)

(b) Energy distribution (Condition V1a)

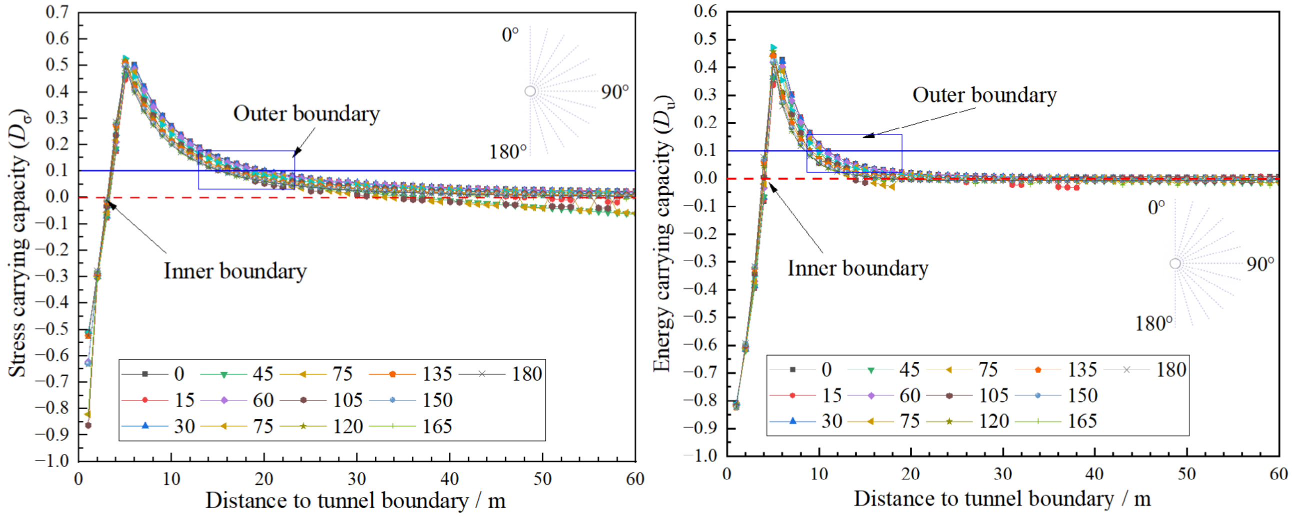

(c) Stress distribution (Condition V1b)

(d) Energy distribution (Condition V1b)

Fig. 7 Load carrying capacity calculation results

the inner and outer boundaries of the stress load-bearing zone were relatively concentrated, as depicted in Fig. 7a and c. The horizontal to vertical stress ratio only affected the load carrying capacity at certain angles and had little impact on the boundary. The redistribution of energy was strongly influenced by the horizontal to vertical stress ratio. When $k \neq 1$, an energy gathering zone could not occur in some directions, and there was no obvious correlation to the stress distribution, as illustrated in Fig. 7b. When $k = 1$, the energy redistribution around the entire tunnel was symmetrical, and the inner and outer boundaries were positioned relatively close together, as shown in Fig. 7d.

The bearing and non-bearing zones surrounding the tunnel were more clearly visible at a depth of 100 m in Grade V surrounding rock mass, as demonstrated by examples V1a, V1b, and V1c in Fig. 8. The corresponding stress concentration area and energy concentration area were calculated through the stress before and after tunnel excavation. Figure 8 is drawn after it was symmetrical. The stress criterion provided a load-bearing zone in the form of a closed curve. When $k = 1$, the inner and outer boundaries were approximately circular. Whereas when $k \neq 1$, the load-bearing zone was elliptical, with the short axis of the inner boundary ellipse parallel to the direction of the major principal stress and the long axis of the outer boundary ellipse parallel to the direction of the major principal stress. The reduction and aggregation zones of energy varied significantly with lateral pressure. The release and gathering zones of energy varied

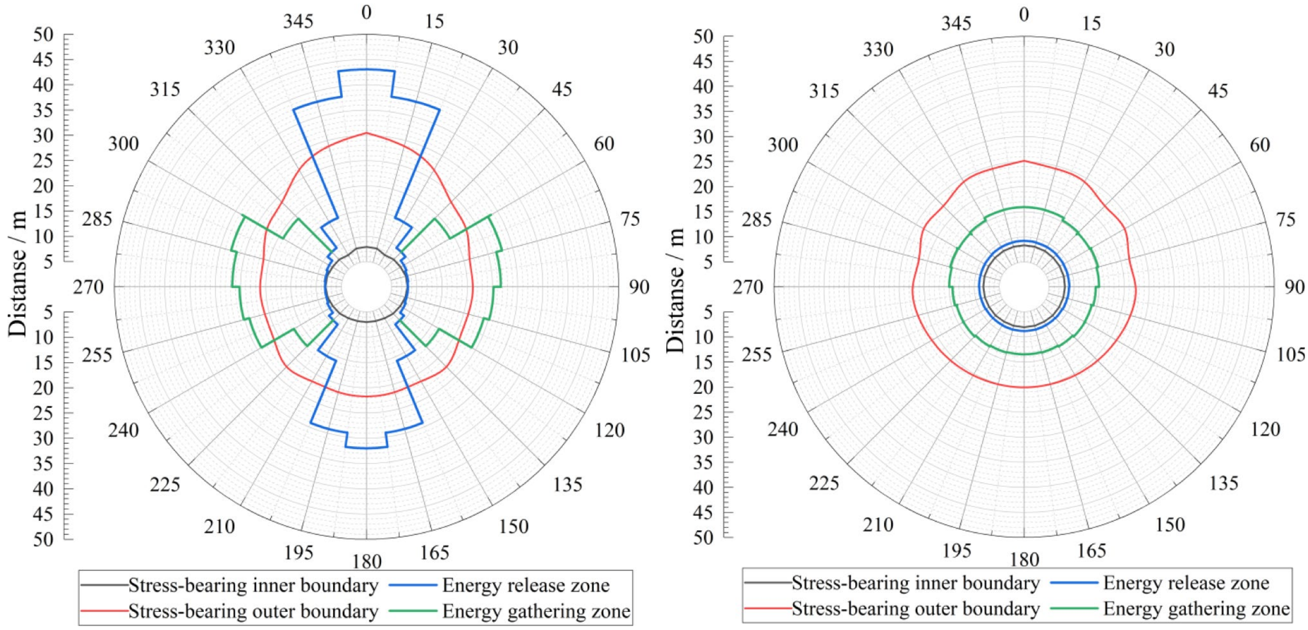

(a) Condition V1a (b) Condition V1b

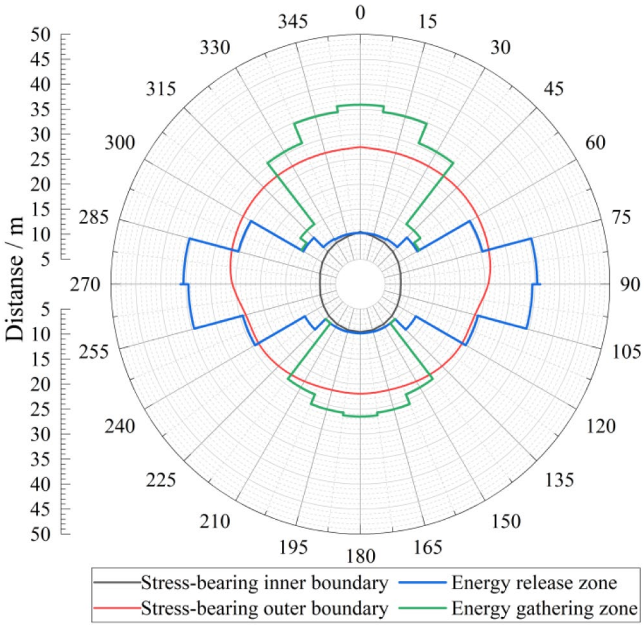

(c) Condition V1c

Fig. 8 Calculation diagram of the load-bearing area

greatly with the horizontal to vertical stress ratio. When $k=1$, the energy redistribution was in a closed circle, with the energy release zone, energy gathering zone, and energy minor influence zone being exhibited in that order, from the tunnel outwards. When $k \neq 1$, the energy gathering zone was distributed along the direction of the major principal stress, and the energy release zone was distributed along the direction of the minor principal stress, which was consistent with the pattern observed in Fig. 2, obtained by Zhu et al. (2003). When the horizontal to vertical stress ratio was equal to 0.5 and 1.5, the energy-affected zone was larger than the stress-affected zone. When the horizontal to vertical stress ratio was equal to 1, the energy-influenced zone was smaller than the stress-influenced zone. Changes in the horizontal to vertical stress ratio had a limited effect on stress redistribution, mainly in terms of localized shape changes. The horizontal to vertical stress ratio had a significant effect on energy redistribution, with the shape and size of the affected area being greatly affected.

4.2 Influencing Factors

4.2.1 Stress Criterion

The load-bearing and non-load-bearing zones of stress around the tunnel were distributed in an approximately circular manner, so the average radius was used for comparison. The inner and outer boundaries were obtained by subtracting the fitted mean radius from the tunnel radius. The thickness of the self-supporting zone was obtained by subtracting the inner radius from the fitted outer radius, as shown in Fig. 9. The different shapes in the figure indicated different overburden depths. The vertical coordinate "Length" showed the average distance from the tunnel boundary to the inner or outer contours of the self-supporting zone. 'Thickness' showed the average distance between the inner and outer boundaries. The size of the inner boundary affected the thickness of the unstable rock mass around the tunnel, while the outer boundary mainly represented the area of influence of the tunnel excavation.

In terms of stress redistribution after tunnel excavation, changing the surrounding rock mass Grade from IV to V led to a large increase in the inner and outer boundaries and the thickness of the self-supporting zone. From the heights of different shapes in Fig. 9, it could be seen that as the depth of the tunnel increased, there was a considerable increase in the inner and outer boundaries and the thickness of the self-supporting zone. The deeper the tunnel is buried, the higher the degree of energy accumulation in the surrounding rock mass after excavation. Therefore, the range of rock mass exceeding the energy storage limit of the rock mass is larger, which is the reason for the increase of the inner boundary of the self-supporting zone. Similarly, as the geostress increases, a larger range of rock masses are required to participate in stress redistribution, resulting in an increase in the thickness of the self-supporting zone. The thickness and inner boundary increase, and the outer boundary of the self-supporting zone also increases. Changes in the overburden depth and surrounding rock mass grade had a more significant effect on the change of the self-supporting zone than changes in the horizontal to vertical stress ratio. For the inner boundary, the higher the horizontal stress, the further it was from the tunnel boundary. For the outer boundary, the closer the horizontal stress was to the vertical stress, the smaller it became, and vice versa. As the outer boundary was larger than the inner boundary, the thickness of the self-supporting zone was mainly influenced by the outer boundary. Thus, the closer the horizontal stress was to the vertical stress, the smaller the thickness of the self-supporting zone. Overall, the surrounding rock mass grade and overburden depth of the tunnel were the primary factors influencing the self-supporting zone of the tunnel, with horizontal stresses having less impact.

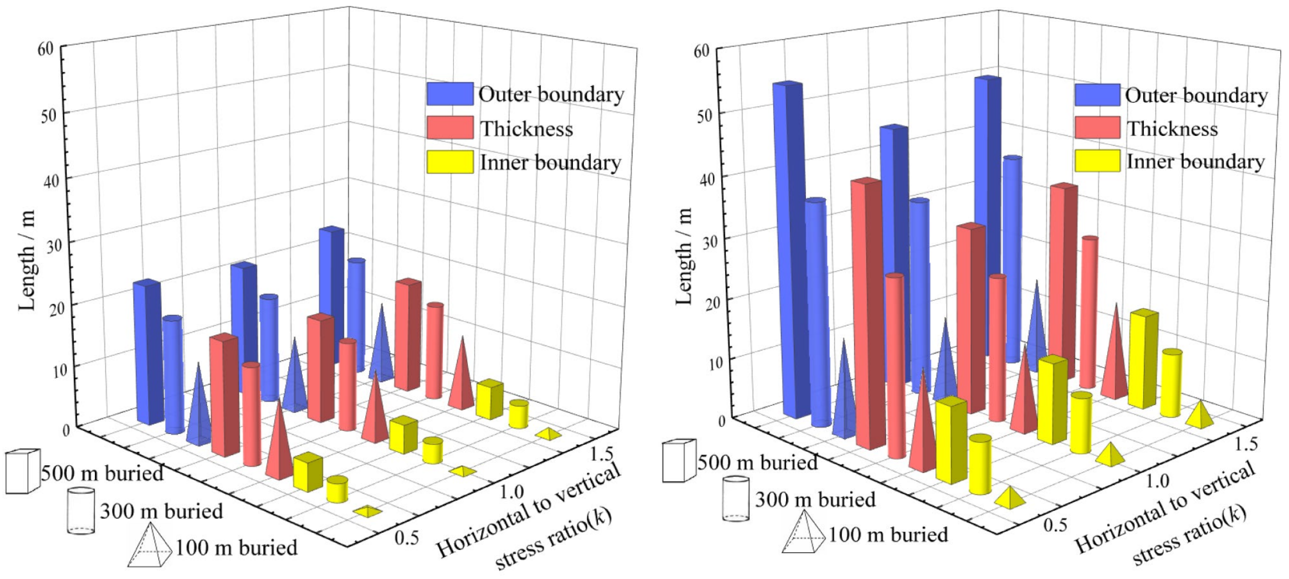

(a) Grade IV

(b) Grade V

Fig. 9 Comparison of the average thickness of the stress criterion

4.2.2 Energy Criterion

Unlike the redistribution of stress, the redistribution of energy was strongly influenced by horizontal stress. Figure 8 shows that the release and gathering of energy had a completely different distribution pattern for the three different horizontal stresses. The parametric analysis of the energy distribution was carried out by separating the individual operating conditions for the three *k* values and the comparison results are shown in Fig. 10. In the case of unequal horizontal and vertical stresses, changes in overburden depth and surrounding rock mass grade would only change the size of the area of the energy gathering and lowering zone and would not affect the shape of their distribution, as shown

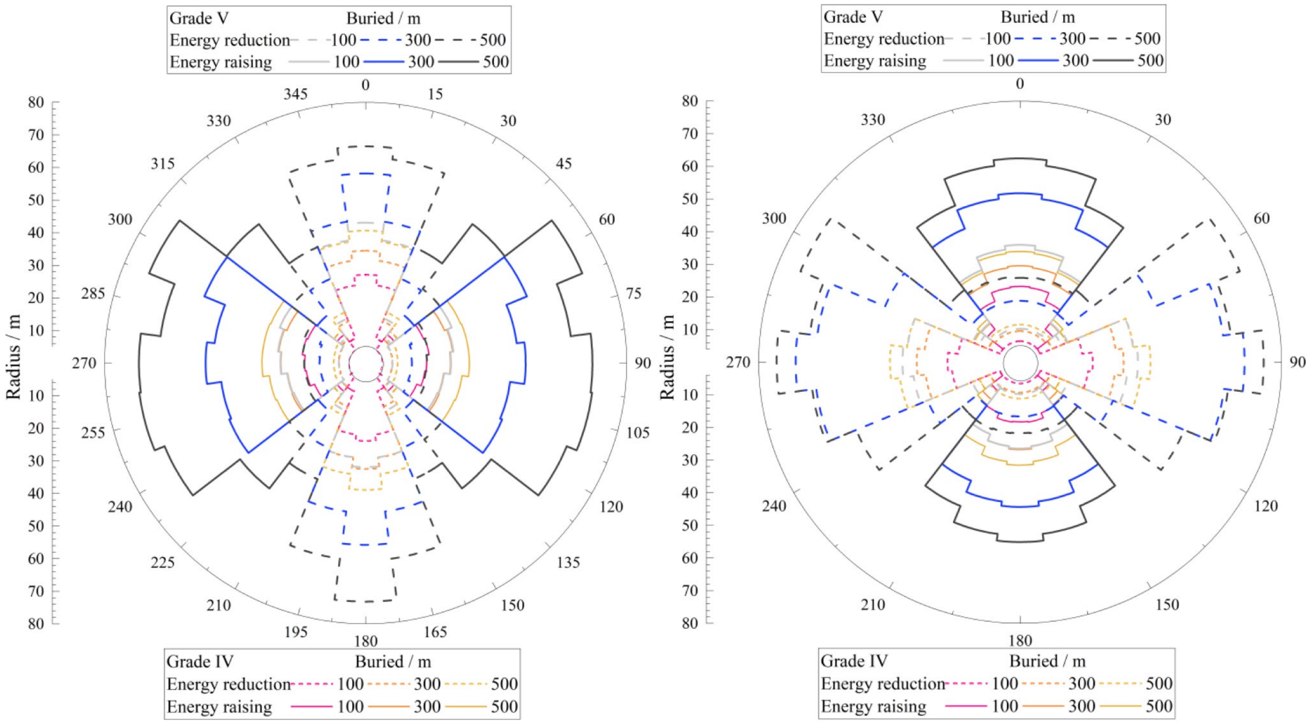

(a) *k*=0.5 (b) *k*=1.5

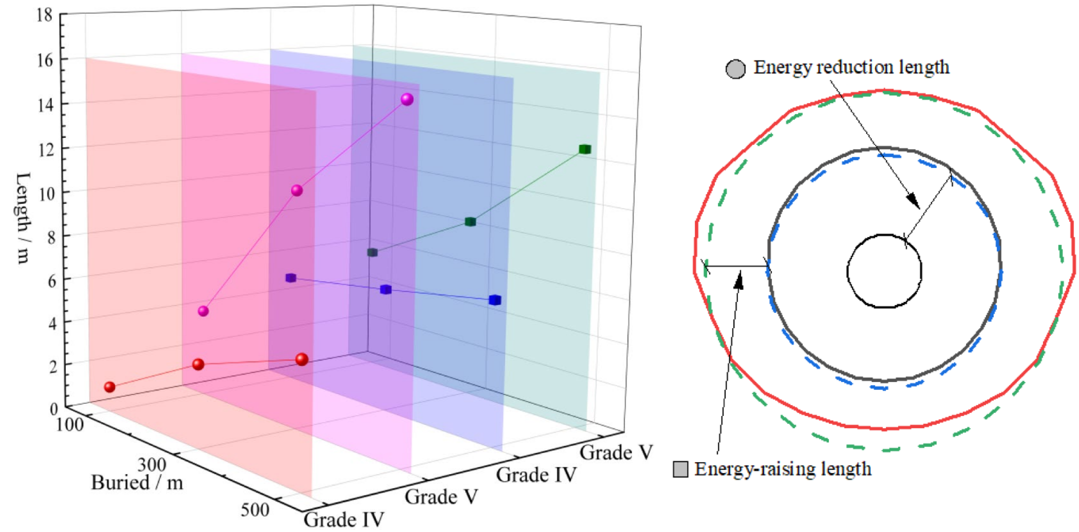

(c) *k*=1.0

Fig. 10 Comparison of energy changes after tunnel excavation in Fig. 10a, b. The energy redistribution of Grade V was overall larger than that of Grade IV. As the depth of burial increased, the zone of energy change gradually increased, with a sudden change at 300 m overburden depth at grade V, where the zone of energy change intensified. When $k = 1$, the energy distribution pattern was consistent with the stress, as shown Fig. 10c. The ball and block are set in Fig. 10c. The ball showed the average distance between the boundary of the bearing area and the tunnel contour. Blocks indicated the average distance between the inner and outer contours of the bearing area. From the tunnel centre outwards, there was the energy reduction zone, then the energy aggregation zone and finally the energy unaffected zone. In the Grade IV surrounding rock mass, the tunnel overburden depth had less influence on the energy change zone. In the Grade V surrounding rock mass, the depth of tunnel burial had a significant effect on the energy change zone. An increase in tunnel depth substantially increased both the energy reduction zone and the energy aggregation zone.

4.3 The Bearing Mechanism

4.3.1 Stress Field Analysis

The principle of force equilibrium states that the product of the total stress and the area under the normal section before and after tunnel excavation must be the same, as shown in Eq. (9). This principle is known as the conservation of stress flow, which means that the stress flow in the surrounding rock mass remains constant in any profile before and after tunnel excavation. Stress flow behaves similar to water flow, where the effective cross-section is reduced and the velocity is increased on either side of the obstacle, but the flow rate remains constant at any cross-section of the flow.

When $k < 1$, vertical stresses predominate and result in vertical cylindrical flow around the tunnel after excavation. A certain divergence of flow occurs above and below the tunnel, and the elastic strain energy of the surrounding rock mass decreases in this region. The flow velocity increases on both sides of the tunnel, and the stress flow lines become denser, causing the elastic strain energy of the surrounding rock mass to gather in this region, as shown in Fig. 11a. The energy release zone around the tunnel is characterized by the energy reduction zone on both sides of the tunnel sidewalls due to the stress flow lines in this area being too dense for the surrounding rock mass to withstand. The elastic strain energy decreases after the rock mass strength enters the peak. The energy reduction in the vertical direction of the tunnel is the result of stress redistribution. Similarly, when $k > 1$, the main stress direction is horizontal, and the same phenomenon as described above occurs, but with a 90° deflection in direction, as shown in Fig. 11c. When $k = 1$, the overall hydrostatic pressure field is present, and the direction of stress flow in the surrounding rock mass after tunnel excavation is from all around to the middle. This flow is slightly affected by gravity, which is negligible. Stress flow gathering occurs around the tunnel, where the energy gathers. When the stress level is too high, or the rock mass is not strong enough, post-peak damage begins to occur around the tunnel perimeter, and the elastic strain energy is reduced, as shown in Fig. 11b. Due to the similar morphological characteristics of a 90° rotation when k is greater than 1 or less than 1, the analysis of the load-bearing mechanism was conducted using $k = 0.5$ and $k = 1$ as examples.

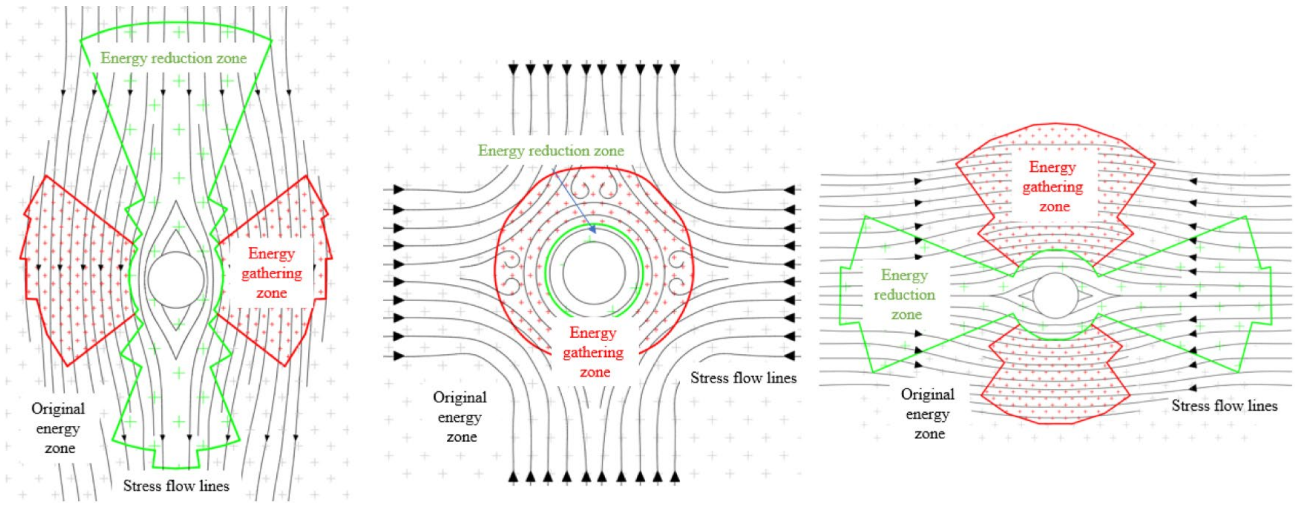

(a) k=0.5 (b) k=1.0 (c) k=1.5

Fig. 11 Energy and stress streamline distribution diagram

$$\int_{S_{\mathrm{h}}} \sigma_{\mathrm{a}} \mathrm{d}x\mathrm{d}y = \int_{S_{\mathrm{h}}'} \sigma_{\mathrm{a}}' \mathrm{d}x\mathrm{d}y, \tag{9}$$

where σ_{a} is the total stress in the rock mass before excavation, vector sum of each principal stress, σ_{a}' is the total stress in the rock mass after excavation, S_{h} is the area of action before excavation, S_{h}' is the area of action after excavation.

4.3.2 Mainly Vertical Stress

In the perpendicular direction of the major principal stress (horizontal direction): The energy concentration zone is located on both sides of the tunnel sidewalls. This situation corresponded to the case of $k = 0.5$, and when $k = 1.5$, the bearing mechanism could rotate by 90°. The changes in the level and overburden depth of the surrounding rock mass would not affect the bearing mechanism, but only the size of the bearing area. This region exhibits high energy and stress concentration, forming an active load-bearing zone that serves as the foundation for the formation of the closed load-bearing zone. This portion is represented by the green Zone I in Fig. 12a. The energy accumulation in this area exceeds the energy limit that the rock mass can withstand, leading to shear failure of the rock mass. As a result, plastic zones appear on both sides of the tunnel, and elastic strain energy is dissipated. This region is unable to bear loads, as depicted by the yellow Zone II on both sides of the tunnel in Fig. 12a. The active load-bearing zone is relatively stable, resulting in a smaller range of deformation impact in the horizontal direction, as shown in Fig. 12c. However, stress concentration will lead to some shear failure, explaining the characteristic distribution of shear plastic zones extending at the sidewalls after tunnel excavation, as shown in Fig. 12b. Figure 12b, c is the calculation cloud maps of working condition V1a.

In the parallel direction of the major principal stress (vertical direction): the energy reduction zones are distributed in a wedge-shaped manner in the upper and lower parts of the tunnel. The active load-bearing zone has a distinctive trumpet-shaped profile. The energy reduction zones are wedged tightly into the active load-bearing zone under the driving force of stress flow (represented by the ground stress vector). The special boundary causes some stress deviation in the energy reduction zones. The tangential stress increases in the deviated portions, transferring the vertical stresses from the upper and lower parts to the active load-bearing zone. This forms a passive load-bearing zone, indicated by the brown Zone III in Fig. 12a, which forms a closed circular ring with the active load-bearing zone. In the vicinity of the tunnel, due to the presence of free faces, the surrounding rock mass will experience a bending-type failure in response to the vertical stresses. Tensile failure zones appear at the boundaries of the tunnel, represented by the red Zone IV in Fig. 12a. The brown zone has a larger area involved in stress transfer and undergoes deformation during the stress transfer process. Consequently, the deformation impact range is significant in the upper and lower parts of the tunnel, as shown in Fig. 12c (vertical direction). The vertical stress adjustment range is large, resulting in lower stress levels in this area. The plastic zone extent is smaller than at the sidewalls, with only localized tensile plastic zones occurring near the tunnel boundaries due to their unique shape. Under the action of vertical stress, part of the rock mass moved towards the tunnel as a whole. During the movement, the bearing zone was formed by wedge tightening.

4.3.3 Hydrostatic Pressure Field

When the vertical stress was equal to the horizontal stress, this situation corresponded to $k = 1.0$. At this stage, the

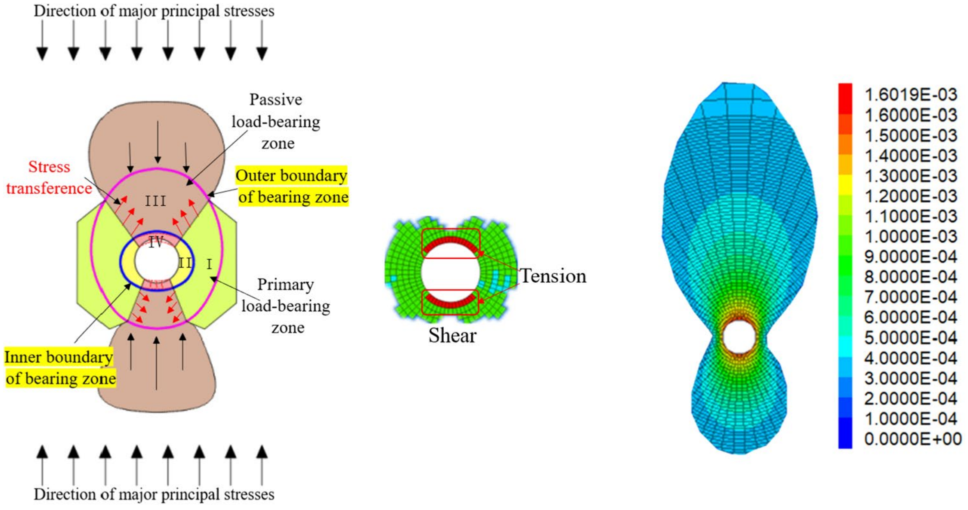

(a) Tunnel load-bearing mechanism (b) Tunnel plastic zone cloud chart (c) Tunnel total displacement cloud chart (m)

Fig. 12 Load-bearing mechanism analysis ($k = 0.5$)

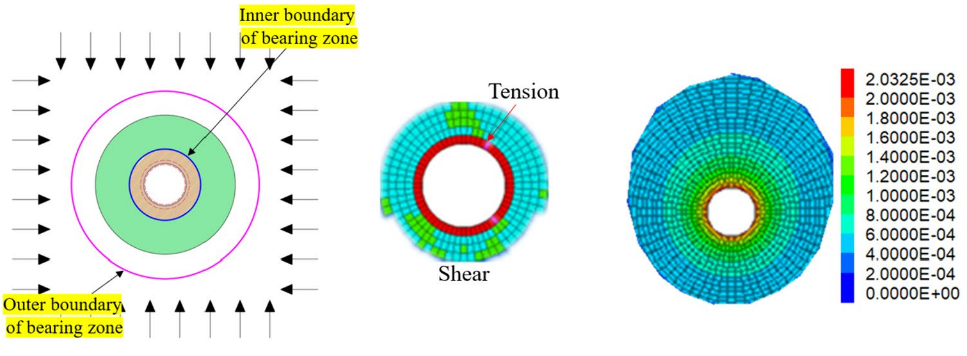

(a) Tunnel load-bearing mechanism (b) Tunnel plastic zone cloud chart (c) Tunnel total displacement cloud chart (m)

Fig. 13 Load-bearing mechanism analysis ($k = 1.0$)

Table 5 Test material properties

Test materials	Number	Height (mm)	Diameter (mm)	Compressive strength (MPa)	Elastic modulus (GPa)	Poisson's ratio
M10 mortar	M1	100.1	49.8	8.75	1.90	0.10
	M2	100.9	50.0	8.93	1.45	0.15
	M3	101.8	50.1	9.26	2.01	0.12

distribution pattern of energy corresponds to the distribution pattern of stress-bearing zones. Both energy and stress exhibit enclosed accumulation zones around the tunnel, which bear the stress release caused by tunnel unloading and contribute to the self-supporting capacity of the tunnel. The rock mass at the far end of the tunnel performs work on the surrounding area under the influence of body forces, leading to energy accumulation around the tunnel and the formation of stress-bearing zones. The outer boundary of the energy concentration zone adopts the initial energy as the standard, which refers to the elastic strain energy at various positions before tunnel excavation. The initial energy is greater than the energy far from the tunnel boundary area in the model. As shown in Fig. 7d, the position of the blue line is higher than the energy at the far end, so the energy accumulation area obtained when using the initial energy as the outer boundary criterion is smaller. Therefore, the area of energy accumulation is smaller than the zone of increased stress, represented by the green region in Fig. 13a. The high stress concentration and unloading effects around the tunnel lead to the occurrence of shear plastic zones, accompanied by increased strain due to the shear failure of the rock mass. This results in a ring of tensile failure zones around the tunnel perimeter, represented by the brown region in Fig. 13a. The deformation pattern of the tunnel also exhibits a divergent distribution from the center to the surrounding areas. The above analysis and the computational cloud maps in Fig. 13b, c are consistent with each other. Figure 13b, c is the calculation cloud maps of working condition V1b.

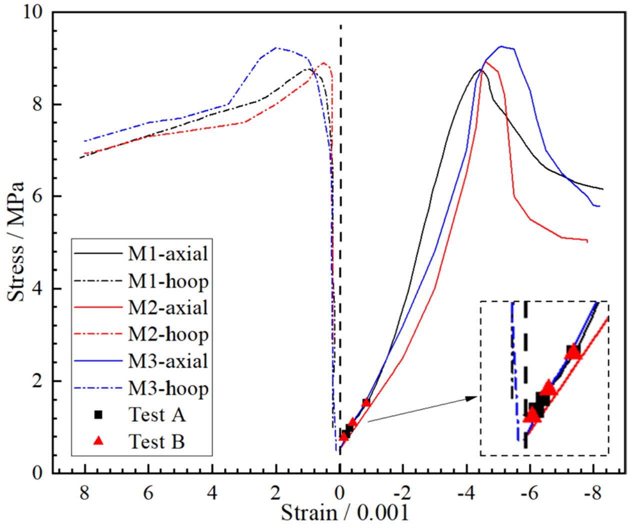

Fig. 14 Stress–strain curve of specimen

4.4 Test Results

4.4.1 Material Strength Calibration

Three conventional uniaxial compression tests were conducted on the experimental casting material. The test results are shown in Table 5, and the stress–strain curve is shown in Fig. 14. It can be observed that the compressive strength of the test material ranged from 8.75 to 9.26 MPa after curing completion, with an average compressive strength of 8.98 MPa. The elastic modulus ranged from 1.45 to 2.01 GPa, with an average elastic modulus of 1.79 GPa. The peak strain was approximately 0.0045.

4.4.2 Mainly Vertical Stress

The stress concentration process of Group A loading is shown in Fig. 15. It can be observed that, regardless of the loading level, the strain values in the horizontal direction of the tunnel are slightly larger, while the overall concentration range in the vertical direction is larger. Similarly, as shown in Fig. 15a, after the first-level loading, the maximum strain of −0.213 corresponds to a stress of approximately 850 kPa, distributed at stress concentration points around the tunnel. As shown in Fig. 15b, after the second-level loading, the maximum strain of −0.322 corresponds to a stress of approximately 980 kPa, distributed on both sides of the tunnel. As shown in Fig. 15c, after the third-level loading, the maximum strain of −0.858 corresponds to a stress of approximately 1.53 MPa, distributed on both sides of the tunnel. The legend is shown in Fig. 14. Numerically, the experimental results are generally consistent with the concentration level under each loading level, indicating a certain level of accuracy in the experiment.

The surrounding area of the strain cloud plot exhibits certain strain variations, but their magnitudes are far smaller than the strain concentration around the tunnel. Therefore, the strain concentration around the tunnel is extracted and shown in Fig. 16. It can be observed that when the horizontal stress coefficient is not equal to 1, the stress concentration around the tunnel exhibits a regular distribution pattern. In the two quadrants perpendicular to the major principal stress, the maximum stress concentration occurs, but the overall disturbance range of the tunnel is small. In the two quadrants parallel to the major principal stress, the stress concentration values are not significant, but the overall disturbance range of the tunnel gradually increases. With the increase of load, the stress concentration level increases further on both sides of the tunnel, and the influence range in the vertical direction also expands. Moreover, with the increase of load, the influence range in the vertical direction becomes larger than the horizontal direction.

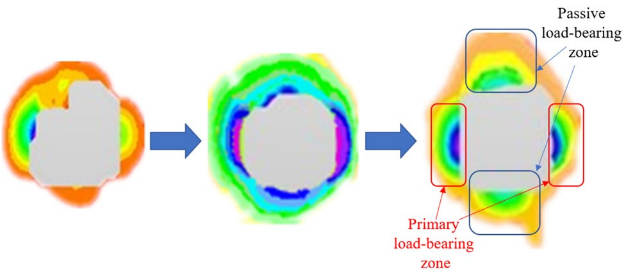

Fig. 16 Evolution of bearing area ($k = 0.5$)

4.4.3 Hydrostatic Pressure Field

The stress concentration process of Group B with uniformly distributed loading on all sides is shown in Fig. 17. It can be observed that regardless of the loading level, a relatively uniform strain (stress) concentration phenomenon is present around the tunnel. In Fig. 17a, it can be seen that after the first level of loading, the maximum strain of −0.137 corresponds to a stress of approximately 780 kPa, distributed at stress concentration points around the tunnel. In Fig. 17(b), it can be seen that after the second level of loading, the maximum strain of −0.418 corresponds to a stress of approximately 1.1 MPa, distributed around the tunnel. In Fig. 17c, it can be seen that after the third level of loading, the maximum strain of -0.844 corresponds to a stress of approximately 1.52 MPa, distributed around the tunnel. It can be observed that the stress redistribution is essentially twice the initial stress, with a slightly higher value due to local stress concentration in the model. Due to the limited load-bearing capacity of the experimental reaction

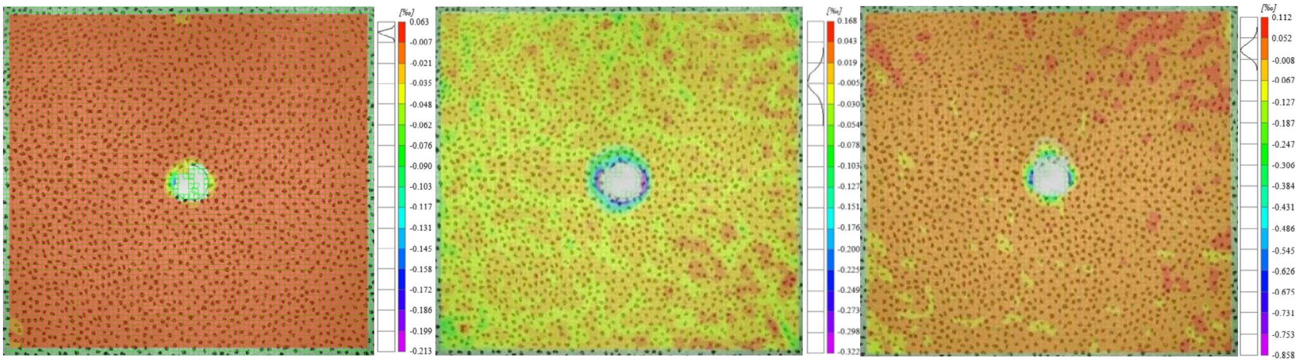

(a) First level loading(‰) (b) Second level loading(‰) (c) Third level loading(‰)

Fig. 15 Test result cloud chart ($k = 0.5$)

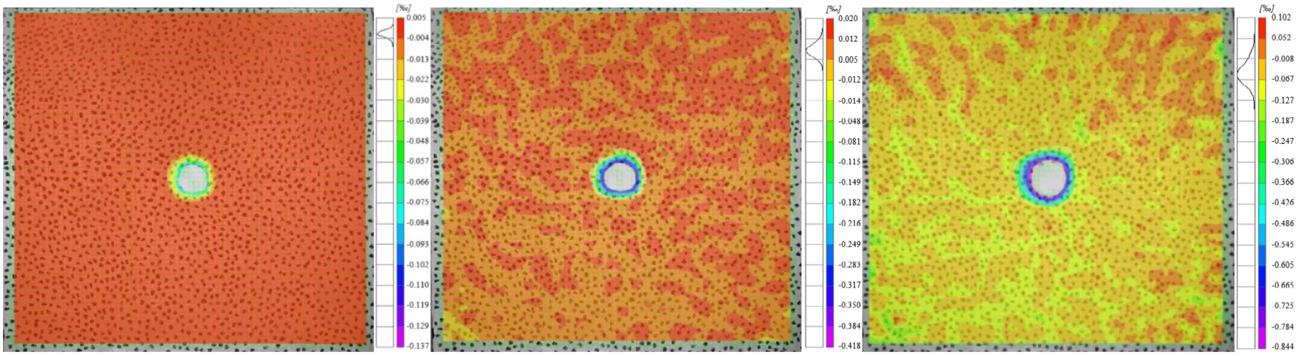

(a) First level loading(‰) (b) Second level loading(‰) (c) Third level loading(‰)

Fig. 17 Test result cloud chart ($k=1$)

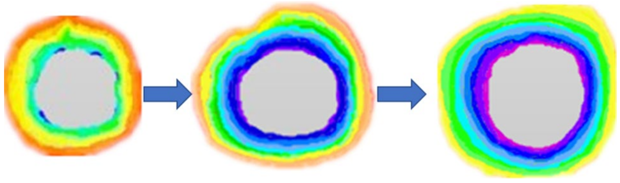

Fig. 18 Evolution of bearing area ($k=1$)

frame, no failure of the test specimens occurred during the experiments.

The surrounding area of the experimental strain cloud diagram exhibited some strain variations, but their magnitudes were much smaller than the strain concentration around the tunnel. Therefore, the strain concentration around the tunnel was extracted as shown in Fig. 18. It can be observed that when the horizontal stress coefficient is 1, the stress concentration around the tunnel exhibits a relatively uniform distribution. With increasing load, the range expands and the stress values gradually increase. The experimental results confirm the analysis presented in Sects. 2 and 3 regarding the strain concentration. The formation of the tunnel's load-bearing zone in a static hydrostatic pressure field is attributed to the work done by the far field on the tunnel cavity, creating a concentrated area of energy/stress around the tunnel. This region serves as the primary load-bearing zone of the tunnel. The observed patterns in the load-bearing zone are consistent in all directions and exhibit axisymmetric characteristics, expanding gradually from the center to the periphery. The stress concentration around the tunnel perimeter also increases further.

5 Conclusions

The FDM was utilized to introduce the stress concentration factor and the energy concentration factor indexes for analysis. The mechanism of tunnel self-supporting zone formation under different horizontal to vertical stress ratios was revealed and verified by experiments. The factors influencing the size of the bearing area were quantitatively analyzed. The study concluded with the following findings.

When k was equal to (close to) 1, the rock mass far from the tunnel worked towards the cavity under the action of the ground stress, resulting in energy accumulation of the surrounding rock mass outside the tunnel contour and in the formation of a bearing zone. The rock mass around the tunnel formed a non-bearing zone due to stress relaxation caused by the accumulated energy exceeding its energy storage limit. When k was not equal to 1, the elastic strain energy of the rock mass accumulated in two quadrants perpendicular to the direction of the major principal stress around the tunnel, forming active bearing zones. The other two quadrants of the rock mass formed passive bearing zones, transmitting stresses to the active bearing zone through the arching effect.

The overburden depth and the quality of the surrounding rock mass affect the size but not the shape of the non-bearing and bearing areas after tunnel excavation. The quality of the surrounding rock mass has a greater influence than the overburden depth. When the Q value of the surrounding rock decreases or when the overburden depth increases, the range of each area becomes significantly larger.

Funding This study was supported by High-Speed Rail Joint-Fund Funded Projects (U2034205) and the National Natural Science Foundation of China Youth Fund (5210082505).

Data Availability Statement Data are available on request to the authors. Everyone can contact Kaimeng Ma (mkm@my.swjtu.edu.cn) to obtain the data.

Declarations

Conflict of interest There is no conflict of interest with other units.

Human rights This study did not involve human participants.

References

An Y, Li J, Liu W, Zhou J, Tan G (2022) Unified boundary determination method of pressure arch in tunnels and its spatial evolution characteristics. China Saf Sci J 32(08):84–90 (**in Chinese**)

Chen CN, Huang WY, Tseng CT (2011) Stress redistribution and ground arch development during tunneling. Tunn Undergr Space Technol 26(1):228–235

Chen RP, Liu QW, Wu HN et al (2020) Effect of particle shape on the development of 2D soil arching. Comput Geotech 125:103662

Chevalier B, Combe G, Villard P (2012) Experimental and discrete element modeling studies of the trapdoor problem: influence of the macro-mechanical frictional parameters. Acta Geotech 7(1):15–39

Cui J, Hou Y, Xie S et al (2023) Analysis and verification of stress and plastic zone in surrounding rocks of hydraulic flushing borehole based on strain-softening. Geomech Geophys Geo-Energy Geo-Resour 9:64. https://doi.org/10.1007/s40948-023-00613-4

Dancygier AN, Karinski YS, Chacha A (2016) A model to assess the response of an arched roof of a lined tunnel. Tunn Undergr Space Technol 56:211–225

Handy BRL (1985) The arch in soil arching. J Geotech Eng II I(3):302–318

Huang Z, Broch E, Lu M (2002) Cavern roof stability—mechanism of arching and stabilization by rockbolting. Tunn Undergr Space Technol 17(3):249–261

Iglesia GR, Einstein HH, Whitman RV (2014) Investigation of soil arching with centrifuge tests. J Geotech Geoenviron Eng 140(2):1–13

Janssen HA (1895) Versuche uber getreidedruck in silozellen. Z Ver Deut Ing 39:1045

Jeon S, Kim J, Seo Y, Hong C (2004) Effect of a fault and weak plane on the stability of a tunnel in rock—a scaled model test and numerical analysis. Int J Rock Mech Min Sci 41:658–663

Keawsawasvong S, Ukritchon B (2020) Design equation for stability of shallow unlined circular tunnels in Hoek-Brown rock masses. Bull Eng Geol Environ 79(8):4167–4190

Kong XX, Liu QS, Zhang QB, Wu YX, Zhao J (2018) A method to estimate the pressure arch formation above underground excavation in rock mass. Tunn Undergr Space Technol 71:382–390

Li K (2010) Pressure arch theory study of horizontal bedded tunnel surrounding rock. Southwest Jiaotong University **(in Chinese)**

Li C (2016) Developing an analytical method to study vertical stress due to soil arching during tunnel construction. Geotech Geol Eng 34(4):1247–1255

Li Y, Zhang D, Fang Q et al (2014) A physical and numerical investigation of the failure mechanism of weak rocks surrounding tunnels. Comput Geotech 61:292–307

Liang XD (2006) Study on arching action by stress adjusting and stability of jointed surrounding rock. China University of Mining and Technology **(in Chinese)**

Lin XT, Chen RP, Wu HN et al (2022a) A composite function model for predicting the ground reaction curve on a trapdoor. Comput Geotech 141:104496

Lin XT, Su D, Shen X et al (2022b) Effect of tunnelling-induced ground loss on the distribution of earth pressure on a deep underground structure. Comput Geotech 147:104781

Ma Y, Lu A, Cai H et al (2022a) A semi-analytical method for elastic-plastic analysis of a deep-buried elliptical tunnel. Comput Geotech 142:104589

Ma K, Zhang J, Dai Y et al (2022b) The calculation for ultimate surrounding earth pressure on deep-buried tunnels in aeolian sand stratum to prevent surface collapse. Bull Eng Geol Environ 81(9):1–17

National Railway Administration of the People's Republic of China (2016) Railway Tunnel Design Code. TB 10003-2016 **(in Chinese)**

Ritter W (1879) Die statik der tunnelgewölbe. Springer, Berlin

Terzaghi K (1946) Rock defects and loads on tunnel supports. Rock tunnelling with steel supports

Tien H (1996) A literature study of the arching effect. M.S. Thesis, Massachusetts Institute of Technology, pp 40–184

Wang CB (2007) Study on the progressive failure mechanism of the surrounding rock of tunnel constructed in soft rock. Tongji University **(in Chinese)**

Wang X, Kang H, Gao F (2021) Numerical study on the formation of pressure arch in bolted gravel plate. Comput Geotech 130:103933

Wu A, Zhao W, Zhang Y, Fu X (2023) A detailed study of the CHN-BQ rock mass classification method and its correlations with RMR and Q system and Hoek–Brown criterion. Int J Rock Mech Min Sci 162:105290

Xu Q, Liu Y, Song YX et al (2021) A method for calculating surrounding rock pressure of deep loess tunnel based on loose broken rock zone theory. Sci Technol Eng 21(23):10054–10060 (**in Chinese**)

Yang JH, Wang SR, Wang YG et al (2015) Analysis of arching mechanism and evolution characteristics of tunnel pressure arch. Jordan J Civ Eng 9(1)

Ye F, Han X, Liu YP et al (2019) Analyze on the dynamic evolution mechanism and rule of pressure arch in tunnel. Chin J Undergr Space Eng 15(1):158–166 (**in Chinese**)

Yi K, Kang H, Ju W, Liu Y, Lu Z (2020) Synergistic effect of strain softening and dilatancy in deep tunnel analysis. Tunn Undergr Space Technol 97:103280

Yi K, Liu Z, Lu Z, Zhang J, Sun Z (2021) Transfer and dissipation of strain energy in surrounding rock of deep roadway considering strain softening and dilatancy. Energy Sci Eng 9(1):27–39

Zhang H, Gong L, Qiu W, Zhao B (2014) Evolution of loosened zone of surrounding rock for tunnels constructed by multi-partition excavation method. Chin J Geotech Eng 36(12):2323–2329 (**in Chinese**)

Zhou P, Wang Z, Lei F et al (2019) Experimental study on mechanical behavior of single-layer lining of steel fiber reinforced concrete tunnel considering interlayer effect. China Civ Eng J 52(05):116–128. https://doi.org/10.15951/j.tmgcxb.2019.05.010. (**in Chinese**)

Zhou P, Jiang Y, Zhou F et al (2022a) Stability evaluation method and support structure optimization of weak and fractured slate tunnel. Rock Mech Rock Eng 55(10):6425–6444

Zhou P, Jiang Y, Zhou F et al (2022b) Study on pressure arch effect of xigeda strata tunnel based on experiment and discrete element simulation. Bull Eng Geol Environ 81(5):1–23

Zhu W, Li S, Bai S et al (2003) Some developments of principles for construction process mechanics and some case history studies. Chin J Rock Mech Eng 22(10):1586–1591 (**in Chinese**)